Edge and sublayer degrees of freedom for phosphorene nanoribbons with twofold-degenerate edge bands via electric field

Yi Ren, Xiaoying Zhou, and Guanghui Zhou [*]

Department of Physics, Key Laboratory for Low-Dimensional Quantum Structures and Quantum Control (Ministry of Education), and Synergetic Innovation Center for Quantum Effects and Applications, Hunan Normal University, Changsha 410081, China

For the pristine phosphorene nanoribbons (PNRs) with edge states, there exist two categories of edge bands near the Fermi energy (E_F), i.e., the shuttle-shaped twofold-degenerate and the near-flat simple degenerate edge bands. However, the usual experimental measurement may not distinguish the difference between the two categories of edge bands. Here we study the varying rule for the edge bands of PNRs under an external electrostatic field. By using the KWANT code based on the tight-binding approach, we find that the twofold-degenerate edge bands can be divided into two separated shuttles until the degeneracy is completely removed and a gap near E_F is opened under a sufficiently strong in-plane electric field. Importantly, each shuttle from the ribbon upper or lower edge outmost atoms is identified according to the local density of states. However, under a small off-plane field the shuttle-shaped bands are easily induced into two near-flat bands contributed from the edge atoms of the top and bottom sublayers, respectively. The evidence provides the edge and sublayer degrees of freedom (DOF) for the PNRs with shuttle-shaped edge bands, which is obviously different from another category of PNRs intrinsically with near-flat edge bands. This is because the former category of ribbons solely have four zigzaglike atomic configurations at the edges in each unit cell, which also results in that the property is robust against the point defect in the ribbon center area. As an application, furthermore, based on this issue we propose a homogenous junction of a shuttle-edge-band PNR attached by two electric gates. Interestingly, the transport property of the junction with field manipulation well reflects the characteristics of the two DOFs. These findings may provide a further understanding on PNRs and initiate new developments in PNR-based electronics.

I. INTRODUCTION

The internal degree of freedom (DOF) of electrons in nanostructures is an important issue of modern condensed matter physics. In addition to the charge and spin DOFs, other ones have also been discussed. For example, in multilayer graphene [1] and transition-metal dichalcogenides (TMDs) [2], both the layer and valley DOFs are presented [3,4]. In addition, new DOF may appear upon tailoring a two-dimensional (2D) material into a nanoribbon. The edge and layer, for instance, have been regarded as tunable equivalents of the spin-one-half DOF in bilayer phosphorene nanoribbons (PNRs) with zigzag edge [5]. However, here we treat the edge and sublayer as two DOFs in a recently revealed monolayer slope-edged PNR (sPNR) with twofold-degenerate edge bands [6].

Phosphorene is a few- or monolayer black phosphorus (BP) where P atoms are arranged in the top and bottom sublayers of a puckered honeycomb lattice [7,8]. Inside phosphorene, each P atom is covalently bonded with three adjacent atoms to form a puckered honeycomb structure due to the sp^3 hybridization [9,10]. This promising new 2D material, in the sense of applications in nanoelectronics, can be exfoliated from bulk BP due to the weak interlayer Van der Waals interaction and possesses a direct band gap of 0.3 eV [7,9]. This direct gap increases up to ∼2 eV as its thickness decreases from bulk to monolayer [11]. In the aspect of application, the field-effect transistor (FET) [7,12–14] based on phosphorene is found to have an on/off ratio up to 10^3 and a high hole carrier mobility to 800 cm^2/Vs [15]. Further, arising from the low symmetric and highly anisotropic structure, phosphorene owns strongly anisotropic electrical, thermal, and optical properties, which may open up possibilities for conceptually new devices [9,16–20].

On the other hand, nanoribbons can offer better tunability in electronic structures because of the quantum confinement and edge morphological influence. Tailoring a 2D phosphorene sheet along the conventional zigzag and armchair directions have been experimentally realized [21,22]. Hence the zigzag PNRs (zPNRs) with significant edge states and armchair PNRs (aPNRs) with a direct band gap have been extensively studied [10,23–26], and their skewed or beard counterparts have also been further reported [24,27]. In general, the edge states projecting to the outermost atoms of a ribbon in real space are near the Fermi level E_F [24,28]. They have been extensively studied for graphene and MoS$_2$ nanoribbons [29,30]. However, a zPNR has two near-degenerate edge bands closing to E_F, which are respectively contributed by the atoms of the two edges. The properties of these important edge states have been recognized [5,28,31–34]. Moreover, we may cut a phosphorene sheet so that the

*ghzhou@hunnu.edu.cn

zigzag (armchair) direction intersects the puckered ridges under a chiral angle other than 0° (90°), resulting in PNRs with other possible edge geometries [6]. These ribbons can be classified into two types, one type with edge states including zPNR and the other without edge states including aPNR. In specification, from our previous definition of the chiral vector $T = ma_1/2 + na_2/2$ for the crystallographic characterizations on planar phosphorene with chiral numbers (m, n), the cases of $m+n=$even integer have defined all possible planar crystal directions [6]. Hence a ribbon can be generally denoted as (m, n)PNR. Furthermore, according to the edge atomic arrangement (morphology), PNRs with edge states can be further divided into two categories. When both m and n are odd, the outermost edge atoms of a PNR are alternately located at the two sublayers, resulting in the shuttle-shaped twofold-degenerate edge bands near E_F, such as (1,3)PNR and (3,1)PNR [6,27,35,36], while for both even m and n, the outermost atoms are located at the same sublayer and the ribbon only has a near-flat degenerate edge band, such as (2,4)PNR and (4,2)PNR [6]. Some of the typical ribbons with these two categories of edge states have already been observed in experiments [37,38]. However, the electronic property may be significantly different from each other between the two categories. There are few studies on the PNRs with shuttle-shaped twofold-degenerate edge bands [27]. Therefore, it is essentially demanded to explore the microscopic origin of the twofold-degenerate edge bands, especially the transport property. Meanwhile, the defects in PNR samples, such as monatomic vacancies, are inevitable in experiments [39]. It is also important to understand the defect effect on the electronic and transport properties [40].

In this paper we select two sPNRs, (1,3)PNR and (2,4)PNR, as the exemplary ribbons belonging to the categories with twofold-degenerate and near-flat degenerate edge bands, respectively. By using the KWANT software within the framework of tight-binding method, we find that the two shuttle-shaped twofold-degenerate edge bands of (1,3)PNR are separated until the degeneracy is removed and a gap near E_F is opened under a sufficiently strong in-plane electric field. Each shuttle contributed from the outmost atoms of the ribbon upper or lower edge are identified according to the local density of states (LDOS). However, under a small off-plane field the shuttle-shape bands are easily separated into two degenerated near-flat bands contributed from the edge atoms of the top or bottom sublayer. The edge band variation with external field for this category is completely different from that of (2,4)PNR belonging to the previously reported zPNR category. This is because a (1,3)PNR has four zigzag atomic configurations on the upper and lower edges and the degenerate bands are from the outermost atoms in the same sublayer or different upper-lower edge. This allows the two DOFs to be distinguished and regulated by applying electric field along different directions. Further, based on this issue we propose a (1,3)PNR homogenous junction attached by electric gates. Interestingly, the transport property of the junction with field manipulation well reflects the characteristics of the two DOFs for (1,3)PNR category. In addition, the defect effect on the transport property is also discussed. The conclusion is that both DOFs are robust against the defect in the center area of the ribbon, but the sublayer DOF is more effective to resist the

edge vacancy than the edge DOF. These results may provide a further understanding on PNRs and initiate new developments in PNR-based electronics.

The organization of the paper is as follows. First, we classify the categories of the PNRs with edge states and then analyze their edge atomic arrangements and unit cell choice. In Sec. II, we present the model description and the details on the calculations. Then in Sec. III, we demonstrate the the edge state bands of the two exemplary sPNRs belong to different categories and the edge band variations under in- and off-plane electric fields, respectively. Hence according to the coexistence of two (upper or lower edge and sublayer) DOFs in monolayer (1,3)PNR, with which a *p-n* junction is proposed and the the important transport property is discussed. Finally, the conclusion is briefly drawn in Sec. IV.
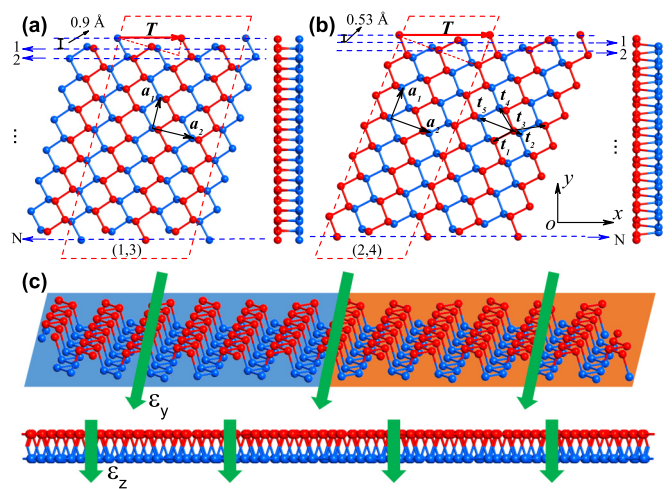

FIG. 1. The schematic illustrations of (a) (1,3)PNR and (b) (2,4)PNR, where the red dashed line parallelogram in each ribbon indicates its minimum periodical supercell, the chiral vector T is illustrated by the red solid arrow along the edge, a_1 and a_2 denote the primitive vectors, and t_1–t_5 are the five effective hoping parameters. The distance between atomic rows for the two sPNRs is 0.9 Å and 0.53 Å, respectively. The ribbon end side views in (a) and (b) indicate the top/bottom sublayer by the red/blue color. (c) The sketch of the *p-n* junction composed of a (1,3)PNR where the different color shade in two sides implies the top and bottom back gates which adjust the Fermi level, and the green thick arrows indicate the in-plane transverse and off-plane vertical electric fields, respectively.

II. MODEL DESCRIPTION AND METHOD

The schematic illustrations of the considered (1,3)PNR and (2,4)PNR are shown in Figs. 1(a) and 1(b), respectively. The red dashed parallelograms are the minimum supercells, where the red solid arrows are the chiral vectors indicating the crystal direction of the ribbon edges [6]. The integer N denotes the number of atomic chains (blue dashed lines) across the ribbon width. Further, for (1,3)PNR shown in Fig. 1(a), the red and blue outmost edge atoms are arranged alternately on the two sublayers (see the side view), as a consequence the supercell width must be twice that of $|T|$. In contrast, the outmost edge atoms for (2,4)PNR are always located at one sublayer and the supercell width is equal to $|T|$. Moreover, as shown in

Fig. 1(c), we propose a homogenous *p-n* junction based on a (1,3)PNR, where the blue and orange background imply the positive and negative potentials provided by back-gate electric gates, respectively. The thick green arrows in upper and lower panels indicate the in-plane transverse electric field along the *y* direction and the off-plane vertical one along the *z* direction, respectively. The stability of PNRs have been analyzed in our previous work [6]. Since $|T|$ of the two selected PNRs here are much less than 20 Å, they are considered relatively stable and do not appear to have obvious edge reconstruction.

We use the KWANT code based on tight-binding (TB) Hamiltonian [41] to calculate the electronic energy band for the selected PNRs, and the atomistic quantum-transport simulations for the proposed junction are based on the scattering-matrix method from matching wave functions [42–44]. In comparison with the first-principles calculation [33], this approach can treat large nanostructures matching the usual experimentally reachable sample size up to sub-100 nm scales with better precision without large computational consumption.

The TB model Hamiltonian for phosphorene [45] in the presence of an electric field can be described as

$$H = \sum_{<i,j>} t_{ij} c_i^{\dagger} c_j + (el\varepsilon_{y/z} + U_i) \sum_i c_i^{\dagger} c_i , \quad (1)$$

where $c_i^{\dagger}(c_j)$ is the creation (annihilation) operator of electron at site $i(j)$, the summation $\langle i,j \rangle$ means over all the neighboring atomic sites with hopping integrals t_{ij}, l is the component of the atomic position from the selected origin along the electric field direction, $\varepsilon_{y/z}$ is the strength of the field along the y/z direction as shown in Fig. 1(c), and U_i is the impurity-induced potential if available. It has been shown that five hopping parameters [see Fig. 1(b)] are enough to describe the electronic band structure of phosphorene. The values of these hopping integrals suggested in previous studies [45] are $t_1 = -1.220$ eV, $t_2 = 3.665$ eV, $t_3 = -0.205$ eV, $t_4 = -0.105$ eV, and $t_5 = -0.055$ eV. Therefore, by solving the discrete Schrödinger equation corresponding to Hamiltonian (1) on the proper basis for the supercell drawn by the red dashed parallelograms in Fig. 1 and applying the Bloch theorem, the *k*-dependent Hamiltonian for a PNR can be written as $H(k) = H_{0,0} + H_{0,1}e^{ika} + H_{0,1}^{\dagger}e^{-ika}$ in the form of $(N' \times N')$ dimensional matrix. Here N' is the number of atoms in the supercell, $H_{0,0}$ is the matrix of the central cell, $H_{0,1}$ the coupling matrix with the right-hand adjacent cell, and *a* is the length between two nearest-neighbor cells. Diagonalizing this *k*-dependent Hamiltonian, we can obtain the band spectrum and the corresponding eigenwave functions. Then we can calculate the LDOS using the following formula

$$\text{LDOS}(E, r) = \frac{1}{c\sqrt{2\pi}} \sum_n |\Psi_n(r)|^2 e^{\frac{-(E_n-E)^2}{2c^2}}, \quad (2)$$

where *c* is the broadening parameter, $\Psi_n(r)$ and E_n are the eigenwave function and eigenvalue, respectively, in which *n* denotes the energy band index and *r* the atom position.

In addition, we mention that the description of the TB model has been effectively used for PNRs with different edge geometries [5,6,20,25,27,28]. We have verified the validity of TB approach by the first-principles calculation using the

Atomistix Toolkit code [46]. The result shows that the edge bands can also be near the Fermi energy and the difference between them is quantitative. As for the influence of spin polarization, it is found that the total energy of (1,3)PNR for the spin polarization case is 8.82 meV lower than that of the nonpolarized case. For the (2,4)PNR, the energy difference is only 0.04 meV. This is well conceivable that the few-meV energy difference will be mitigated by a reasonable finite temperature (few tens of Kelvin), i.e., the spin-polarized states will transit into paramagnetic states in actual experiments so that we do not consider the effect of spin polarization on the results for the present work.

In calculating the conductance for the junction under an external electric field, it is divided into the left electrode, the right electrode, and the middle scattering region. The *S* matrix can be obtained by matching the wave functions at the two interfaces of the electrode/scattering region. Once the *S* matrix is obtained, the conductance of the system at zero temperature can be calculated by using the Landauer formula [47]

$$G_{LR} = \frac{e^2}{h} T_{LR} = \frac{e^2}{h} \sum_{n \in L, m \in R} |S_{mn}|^2, \quad (3)$$

where L/R labels the left/right leads, T_{LR} is the transmission coefficient from lead L to R, and S_{mn} gives the scattering amplitude from an incoming mode *n* to an outgoing mode *m*, both of which are the elements of the scattering matrix. It is clear that the conductance depends on the number of available transport modes through the junction.

III. RESULTS AND DISCUSSIONS

A. Edge bands under in-plane electric field

The calculated energy spectra for the selected exemplary (1,3)PNR ($N = 35$) and (2,4)PNR ($N = 49$) with nearly the same width ~3 nm under an in-plane electric field with different strength are shown in Figs. 2(a)–2(c) and 2(d)–2(f), respectively, where the Fermi level E_F is set to zero. The left and right insets in (b), (c), and (f) indicate the LDOS corresponding to energies marked, respectively, by the red and blue points contributed by the ribbon upper or lower edge outermost atoms, where the side view for each supercell is embodied. First, as shown in Fig. 2(a), the band structure of the pristine (1,3)PNR has a shuttle-shaped edge band near E_F, which implies the ribbon is metallic. In fact, the shuttle-shaped edge bands are twofold degenerate differentiating by the red dashed and blue solid lines. However, the degeneracy can be eliminated by applying an in-plane electric field along the *y* direction. As a small field with strength $\varepsilon_y = 2$ mV/Å is applied shown in Fig. 2(b), the twofold-degenerated edge bands obviously separate into two partially overlapped shuttles. Interestingly, as shown in Fig. 2(c), the two shuttles are completely separated as the field strength is further increased up to 5 mV/Å, which means the degeneracy is completely removed. In contrast, for the (2,4)PNR as the example of the another category, it has two near-flat degenerate edge state bands in the original band structure which are drawn by the red dashed and blue solid lines shown in Fig. 2(d). They also pass through E_F exhibiting metallicity, which is very similar
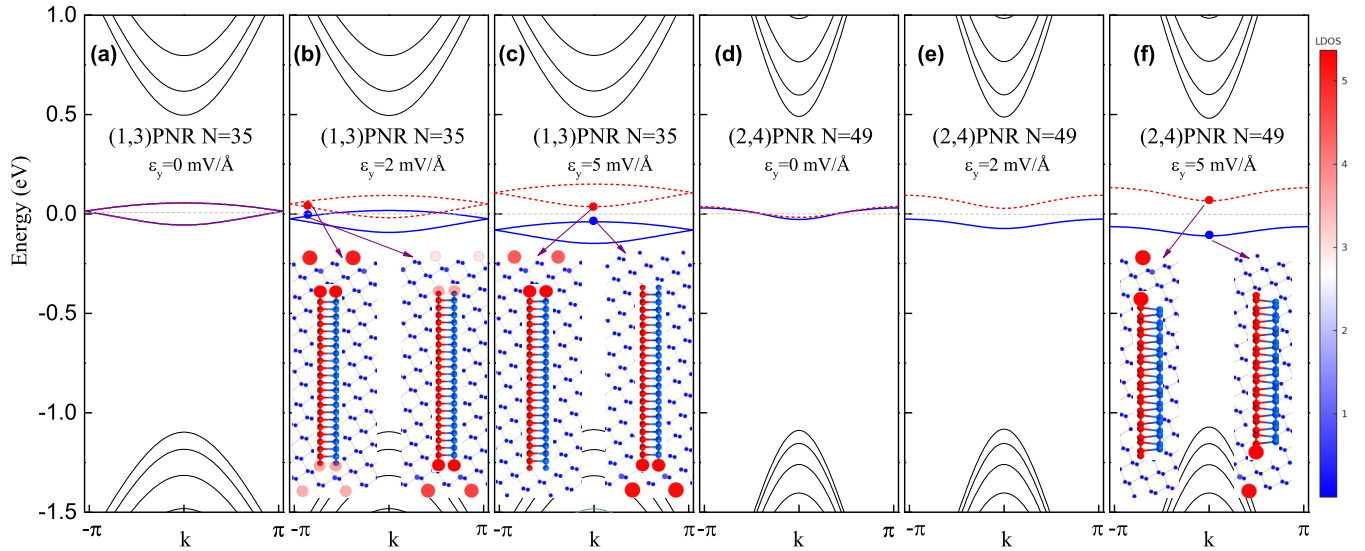
FIG. 2. The band structure for (a)–(c) (1,3)PNR with $N = 35$ and (d)–(f) (2,4)PNR with $N = 49$ under an in-plane electric field with different strengths, (a) and (d) $\varepsilon_y = 0$, (b) and (e) 2 mV/Å, and (c) and (f) 5 mV/Å, respectively. The Fermi energy E_F is set to zero, and the left and right insets in (b), (c), and (f) indicate the LDOS distributions corresponding to energies near E_F marked by the red and blue points, respectively, where the side view for each supercell LDOS is embodied. The right-side attached color bar indicates the electron density from the lowest (blue) to the highest (red) value.

to that of a conventional zPNR except for a little difference in the curvature of the edge bands [10,24,48]. However, much different from the twofold-degenerated bands, the degeneracy for this category of ribbon can be easily removed by a small electric field as shown in Figs. 2(e) and 2(f). The characteristic of edge band under an electric field for (2,4)PNR is very similar to the extensively studied zPNR [24,28,49], and hence we attribute them to the same category.

An in-plane electric field removing the degeneracy of the edge bands can be understood from Hamiltonian (1). The additional diagonal terms increase (accumulate) linearly with the y coordinate. From the analysis of the calculated results, it can be seen that the degenerate edge state bands for both categories of sPNRs would be broken by the application of an in-plane electric field. As the field strength increases, a band gap is opened and the transition from metal to semiconductor is occurred. The variation of (2,4)PNR edge bands with electric field is basically the same as zPNR [24,28,49]. This is because they belong to the same category of sPNRs, where the outermost atoms of the ribbon are all at the same sublayer. However, for the (1,3)PNR with twofold-degenerate edge bands, the E_F is embedded in a mirrored shuttle-shape bands. In order to further know which atoms in the ribbon contribute the edge state bands, we have calculated the LDOS at the energies near E_F marked by the red and blue points, respectively. When the two shuttle-shape bands are not completely separated shown in Fig. 2(b) for $\varepsilon_y = 2$ mV/Å, from the insets we see the difference in LDOS between energies on the two shuttles. The red/blue dashed/solid shuttle bands are mainly contributed by the outermost atoms at the upper/lower edge.

In addition, the left and right insets in Figs. 2(c) and 2(f) depict the real-space electronic distributions at the energies of conduction band minimum (CBM) and valence band maximum (VBM) marked by the red and blue points, respectively.

The right-side attached color bar indicates the density from the lowest (blue) to highest (red) value. From the LDOS insets we can identify whether an edge band is completely contributed by the outmost atoms of the upper or lower edge of the ribbon, which provides a (upper-lower) edge DOF. However, we cannot distinguish them from which sublayers since their responses to an in-plane field are the same. Therefore, we need to apply an off-plane vertical electric field along the z direction, respectively, to the two categories of sPNRs.

B. Edge bands under off-plane electric field

The difference in the layer atomic arrangement on the edge of a sPNR with different parity rows can be reflected by the response to an off-plane electric field and then affects the corresponding band structure. This effect has been revealed and discussed for other 2D material nanoribbons, such as graphene, silicene, and phosphorene ones [28,50,51]. Here, in Fig. 3 we present the result of the edge band response to a vertical electric field with strengths $\varepsilon_z = 0.1$ and 0.4 V/Å for the two exemplary ribbons, respectively. For the consideration of the even-odd parity [20,28], we consider the two width cases of $N = 35$, 36 and $N = 49$, 50 for (1,3)PNR and (2,4)PNR, respectively. The LDOS left/right inset corresponding to the energies marked by the red/blue point. From Fig. 3(a) for (1,3)PNR with $N = 35$, the twofold-degenerate edge bands in shuttle shape are almost unchanged under small $\varepsilon_z = 0.1$ V/Å. However, when ε_z is increased up to 0.4 V/Å, interestingly, the two shuttle-shape edge bands are separated into two nearly flat bands as shown in Fig. 3(b). This results in implying a transition from metal to semiconductor phase. But the twofold degenerate is still not removed. Further, from Figs. 3(a)–3(d) it seems that the number of atom rows (parity) does not affect the band structure of (1,3)PNR. In addition, the side view in (b) shows that the left/right inserted LDOS come
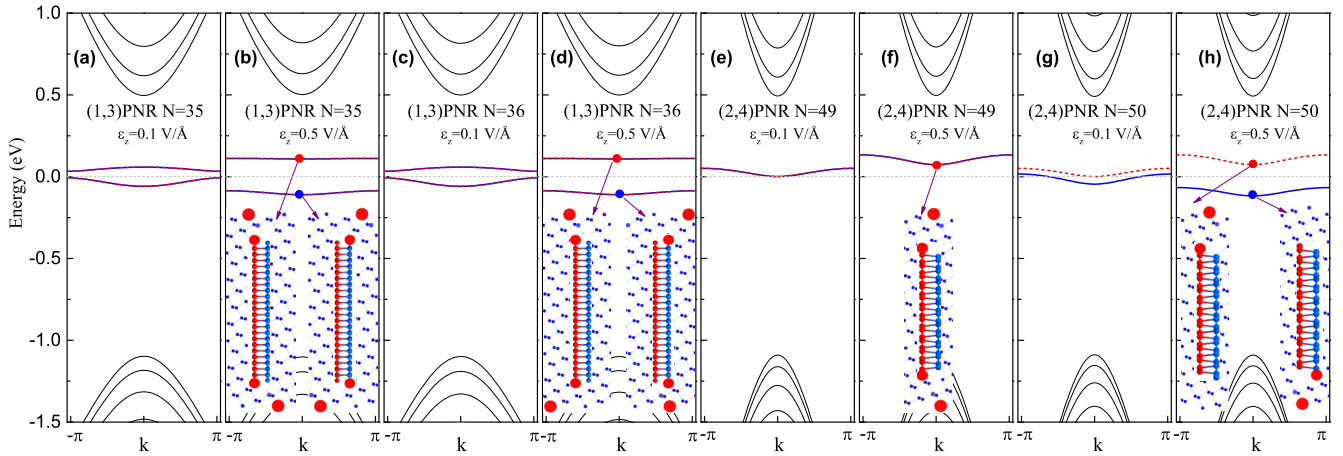
FIG. 3. The band structures for (a)–(d) (1,3)PNR with odd ($N = 35$) and even ($N = 36$) parities under an off-plane vertical electric field with different strengths, respectively, where (a) and (c) $\varepsilon_z = 0.1$ V/Å and (b) and (d) 0.5 V/Å. The band structures for odd-even ($N = 49$–50) (2,4)PNR under the same field are correspondingly shown in (e)–(h). The insets in (b), (d), (f), and (h) depict the LDOS distributions corresponding to the edge states at the certain energies pointed by the red and blue points, where the side view for each supercell LDOS is embodied. The color bar indicating the density is neglected here since it is the same as that in Fig. 2.

from the edge outermost atoms of the top/bottom sublayer. We can identify a band from the top or bottom sublayer, which provides a sublayer DOF. This is because the edge outmost atoms are alternately located at the top and bottom sublayers. In the contrast, for (2,4)PNR belongs to another category with two near-degenerate edge bands, the response of the edge bands to the field is sensitive on the ribbon width (parity), which is the same as that for the conventional zPNRs [28]. As shown in Figs. 3(e) and 3(f), in specification, with the increase of the field strength the edge band degeneracy of the odd-numbered ($N = 49$) ribbon can not be broken but moves upward a little, since the degenerate edge bands are contributed by the outermost atoms of both edges. However, for the even-numbered ($N = 50$) ribbon shown in Figs. 3(g) and 3(h), the outermost atoms of the two edges come from the same sublayer. Hence as the field strength increases, the edge band degeneracy is removed and the transition from metal to semiconductor occurs.

C. (1,3)PNR homogeneous junction

Next, from the above results for the two exemplary sPNRs belonging to different categories, we know that a monolayer (1,3)PNR owns two DOFs of edge and sublayer, which is particularly similar to a bilayer zPNR with two DOFs of edge and layer [5]. Using this similarity, we may construct a homogenous *p-n* junction using a (1,3)PNR. The two sides of a (1,3)PNR are attached by the near top and bottom back gates which adjust the E_F, leading to the lifting up or down of the edge bands for two ends. Further, the external in-plane and off-plane electric fields applied on the junction shown in Fig. 1(c) can be realized by using a side-gate and another back-gate electrode, respectively. The side-gate technique has been proven to be experimentally feasible in graphene as a channel material for other applications [52,53]. The back gates can arouse a potential difference (electric field) across the whole monolayer. This kind of setup has been realized for bulk phosphorene transistors [54,55]. A pseudospin

field effect transistor has also been proposed and characterized based on a bilayer zPNR-based junction, in which a pseudospin-polarized current is generated [5]. The similar interesting effect may also be realized in the *p-n* junction based on a monolayer (1,3)PNR, which can generate an edge- or sublayer-polarized current by properly adjusting the gate electrodes.

In Fig. 4(a), we show the calculated conductance spectrum for the proposed junction based on (1,3)PNR with a width ∼3 nm under a transverse in-plane field with different strengths $\varepsilon_y = 0$ (gray line), 0.5 (blue), and 5 mV/Å (red), respectively. The solid/dashed line indicates the alignment for the edge bands from the same/different upper-lower edge. The separated edge bands from the two edges of the terminals with/without alignment by back gates is shown in Fig. 4(c), where the upper/lower panel corresponds to the case of the solid/dashed line in 4(a), and the green/red arrows implies the switch on/off state. First, we find a conductance plateau of $2e^2/h$ around E_F for the junction without external field shown by the gray solid line, which is in accord with the band structure for a pristine (1,3)PNR shown in Fig. 2(a). When a small field 0.5 mV/Å is applied, by adjusting the positive and negative voltages of the two back gate as to the edge bands from the same upper or lower edge be aligned, the conductance still maintains a $2e^2/h$ plateau (blue solid line) near E_F, whereas the conductance is decreased to $0.3e^2/h$ from different edge as shown by the blue dot-dashed line. This is because the band degeneracy is broken not enough so that the two shuttle-shaped edge bands are not completely separated. Further, as the field strength increases up to 5 mV/Å, the degenerate shuttle-shaped edge bands is fully removed and a significant band gap is opened around E_F [see Fig. 2(c)]. As a consequence, when the same edge bands are aligned as shown in the upper panel in 4(c), a conductance gap correspondingly appears with two $2e^2/h$ plateaus beside it (red solid line). Otherwise the conductance is almost zero even though there are two shuttle-shaped edge bands from the different upper or
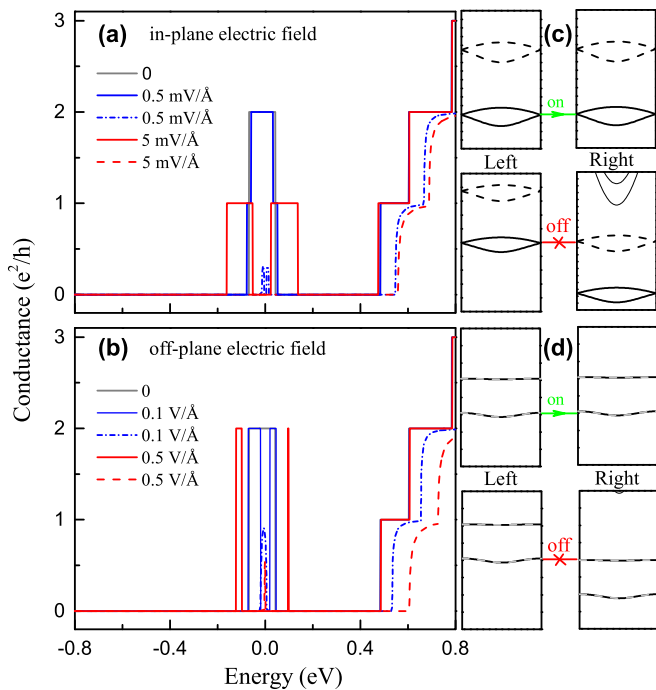
FIG. 4. The conductance spectrum for the (1,3)PNR-based *p-n* junction with a width about 3 nm under (a) in-plane transverse and (b) off-plane vertical electric fields, respectively. The gray solid line implies the conductance without applied field. The blue and red solid (dashed) lines indicate the edge bands from the same (different) (a) upper-lower edge with field strength 0.5 and 0.5 mV/Å, (b) top-bottom sublayer with field strength 0.1 and 0.5 V/Å are aligned, respectively. (c) and (d) The alignment of the edge bands of the two semi-infinitive ribbons under transverse and vertical fields, respectively, where the green/red arrow implies the on/off state of the junction.

lower edge are aligned as shown in the lower panel in 4(c), which shows a transport off state.

Since the speciality of the edge atom arrangement for the monolayer (1,3)PNR, sublayer is also an important DOF in its transport property. In Fig. 4(b), we show the conductance spectrum for the junction under an off-plane vertical electric field with strengths, 0 (gray), 0.1 (blue), and 0.5 V/Å (red), respectively. Here the solid/dashed lines indicate the two edge bands from the same/different sublayers are aligned, of which the diagrammatic sketch for the edge band alignment is shown in 4(d). First, we also find a conductance plateau of $2e^2/h$ around E_F for the junction without external field shown by the gray solid line. In the presence of applied field $\varepsilon_z = 0.1$ V/Å, there is a gap opened within the shuttle-shaped edge bands. Therefore, as the edge bands from the same upper or lower edge are adjusted (by back gate) to be aligned, the conductance exhibits two steps of $2e^2/h$ besides E_F (see the blue solid line), which is in accord with the band structure shown in Fig. 3(b) or 3(d). In this case the increase of the field strength (e.g., $\varepsilon_z = 0.5$ V/Å) only result in the two narrower steps and more far away from E_F (see the res solid line). On the contrary, when the edge bands from the same upper or lower edge are not aligned, the conductance is nearly zero except for very small peaks at E_F as shown by the blue and red dashed lines. The reason for the results is that the edge
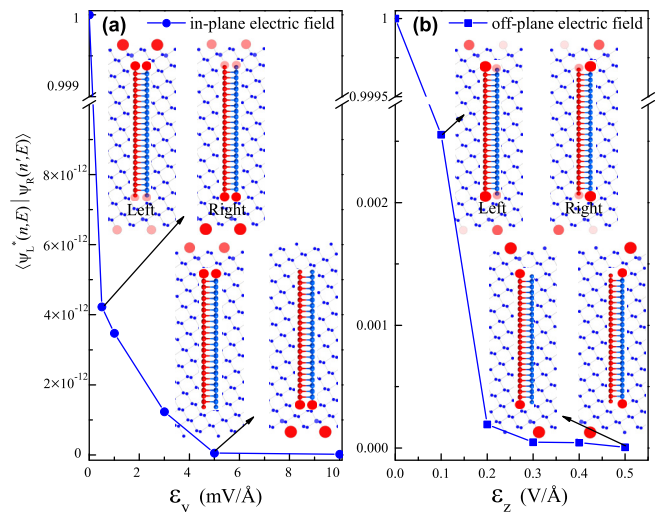

FIG. 5. The wave-function overlap, $< \Psi_L^*(n, E)|\Psi_R(n', E) >$, as a function of (a) ε_y and (b) ε_z for the two terminals of the junction, where n (n') is the band index number for the junction left (right) side. The LDOS diagrams with certain energies at two different field strengths pointed by black arrows are inserted with the embodied side view of the supercell.

outermost atoms of (1,3)PNR are alternately located at the top and bottom sublayers. Therefore, a small vertical electric field can result in a wave function superposition in different sublayers.

In order to further understand the rule of the two DOFs in transport for the junction, in Fig. 5 we plot the dependence of wave-function overlap, $\langle \Psi_L^*(n, E)\Psi_R(n', E)\rangle$, as a function of the field strength (a) ε_y and (b) ε_z. Here $\Psi_{L/R}(n, E)$ is the wave function in the left/right (L/R) side of the junction. The LDOS with certain energies at two different field strengths are also inserted with the embodied side view of the supercell. From Fig. 5, we first note that the overlap value drops rapidly as the field strength increasing due to the degeneracy elimination, with which the edge bands from the different upper-lower edge or top-bottom sublayer are separated. Therefore, without applied field the wave-function overlap is equal to 1. In this case the edge bands are completely superposed, which refers to its pristine state shown in Fig. 2(a). Meanwhile, by adjusting the two back gates as to the two side edge bands from the same edge or sublayer aligned as shown in upper panels of Fig. 4(c) or 4(d), the overlap degree is also equal to 1 regardless of the electric field strength.

Further, as shown in Fig. 5(a), we find that the two shuttle-shaped edge bands from the upper or lower edge are aligned by adjusting the back gates as to the potential difference between the junction two sides is equal to the electric field strength [see the lower panel in Fig. 4(c)], the wave-function overlap for two terminals is greatly reduced. When the two shuttle-shape edge bands are just separated a little by a small field 0.5 mV/Å, the wave-function overlap is greatly reduced to a small value, which corresponds to the blue dashed peaks near E_F in Fig. 4(a). This is because the overall degeneracy of the two shuttle bands would be almost removed even under a small electric field, but some of the degeneracy is still remained. Therefore, at certain energies the superposition of

the wave functions in two sides still has a definitive value. In this case, from the LDOS shown in left upper panel of Fig. 5(a)], we can see it distributes at the upper and lower edge outermost atoms. Specifically, the upper edge atoms in the left side account for the major contribution (bright red spots), while the reddish ones at lower edge indicate a partial contribution. On the contrast, the LDOS distributed are the upper-lower edge for the right side is opposite to the left one. As the field strength is increased up to 5 mV/Å, the wave functions overlap for two side approaches zero (as red dashed line shown in Fig. 4(a)). This is because that the two shuttle edge bands are completely separated, and electrons are localized only at the outmost atoms of one edge. This can also be seen from the LDOS insets with the embodied side view of the supercell. On the other hand, since the edge mostout atoms of (1,3)PNR are alternately arranged on the top and bottom sublayers, the wave functions of the top and bottom sublayer atoms still mix together when a large vertical electric field is applied as shown in the lower inset of Fig. 5(b). Hence the amplitude scale of y axis in Fig. 5(b) is much larger than that in 5(a). Therefore, when $\varepsilon_z = 0.1$ V/Å the wave-function overlap for two sides is still large, which corresponds to the blue dashed plateau near E_F in Fig. 4(b). When the vertical field becomes larger, the wave-function overlap of the top and bottom sublayers tends to zero due to the localization of electrons, as shown by the lower inset in Fig. 5(b) for LDOS with 0.5 V/Å.

Finally, we demonstrate the influence of defect on the transport, which is also very important for device application by using the proposed DOFS since defects are inevitable on PNR samples in experiments [39]. For the sake of argument on the two DOFs in a (1,3)PNR, here we mainly consider two kinds of monatomic vacancies. As shown in the top of Fig. 6 for a defective (1,3)PNR, there are two monatomic vacancy positions indicated by the black dotted circles, one at the edge (EV) and the other in the center (CV) of the ribbon. Figure 6 gives the conductance spectrum, where (a),(c) and (b),(d) for CV and EV cases with $\varepsilon_y = 5$ mV/Å and $\varepsilon_z = 0.1$ V/Å, respectively. As a reference, the red dashed lines in (a),(c) indicate the conductances for a pristine (1,3)PNR without defect but with in- and off-plane fields, respectively, which can be refer to the corresponding energy spectrum shown in Figs. 2 and 3. As is seen from the conductance spectra shown by the blue solid lines, a CV does not affect the edge bands regardless of the field direction, resulting in an unchanged conductance in comparison to the pristine case shown in (a) and (c). But the situation for EV is much different. Comparing with the conductance spectrum shown by the red solid line in Fig. 4(a) for the same upper-lower edge are aligned [also shown by red dashed line in Fig. 6(a)]. As shown in Fig. 6(b), we find that the edge state on one of the edges with an EV is severely weakened, which result in that the conductance plateau on the right side of E_F almost disappears. The original conductance plateau is maintained. In addition, for a EV with $\varepsilon_z = 0.1$ V/Å shown by the blue solid line in Fig. 6(d), the conductance steps are retained as the ideal case [see the blue solid line in Fig. 4(b) and the red dashed line in Fig. 6(c)]. But the conductance peak on the left side of E_F is reduced by half, while the right side peak is still close to $2e^2/h$. This importantly implies that the CV has no effect on the edge state. The same result
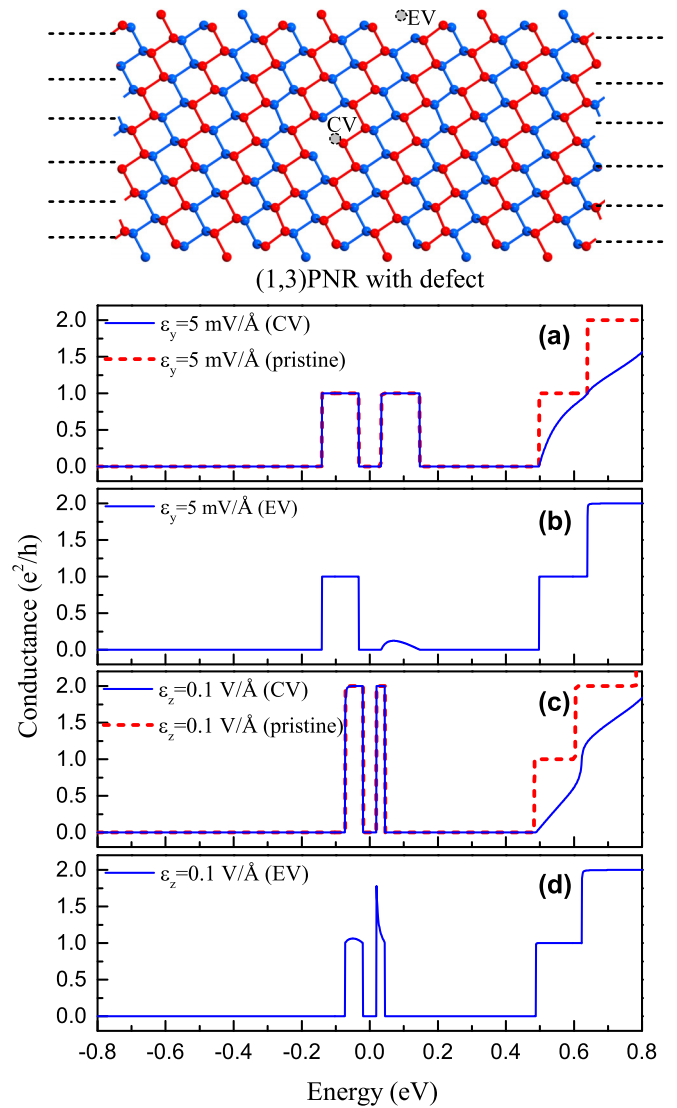

FIG. 6. The conductance spectrum of a (1,3)PNR with monatomic vacancy, respectively, located at the (a),(c) center and (b),(d) edge of the ribbon, where (a),(c) with $\varepsilon_y = 5$ mV/Å and (c),(d) $\varepsilon_z = 0.1$ V/Å. The red dashed line in (a) and (c) corresponds to the pristine case without defect.

is expected for the in-plane field case. Moreover, due to the particularity of the two DOFs, the effect of EV on edge-state contributed conductance is different under the regulation of electric field. As shown by the LDOS in Fig. 5(a), a very small in-plane field can make the outer electrons of the edge atoms localized, which provides the transport channel corresponding to the edge with an EV almost forbidden. On the other hand, a large off-plane field would cause a certain degree of wave-function overlap between the sublayer atoms on the same side [as shown in Fig. 5(b)], so that an EV in one sublayer only destroys the edge state of the corresponding sublayer, while the other sublayer on the same side still maintains a channel. In general, the sPNRs with two DOFs can reduce the influence of low-concentration edge monatomic defects on the edge states to a certain extent.

At last but not least, besides the atomic defects the edge passivation of nanoribbons is also an important issue because

that the edges are usually passivated in real experimental samples. When edge hydrogen (H) passivation is considered in the TB calculation, usually an extra potential field is applied on the edge atoms of the ribbons. This may lead to that the original edge bands are disappeared or modified (see, e.g., Ref. [20]). Here we have also tested the H- and O-passivation cases by using a DFT calculation, respectively. The result shows that the H-passivated edges do not exhibit edge states, while O-passivated ones remain qualitatively similar to the case of bare edges. The result of the edge bands is qualitatively the same as those by the TB approach, which confirms that the device assumption based on (1,3)PNR is scientifically valuable [6].

IV. SUMMARY AND CONCLUSION

In summary, we have studied the difference in electronic structures between the two categories of sPNRs with edge states and the variation under an external electrostatic field. Taking (1,3)PNR and (2,4)PNR as the examples, we first identify the distinction of edge morphology and the unit cell selection for these two ribbons. Then, by using the KWANT code based on the TB approach, we find that the shuttle-shaped twofold-degenerate edge bands of (1,3)PNR can become two separated shuttles until the degeneracy is removed and a gap near E_F is opened under a sufficient strong in-plane electric field. Each shuttle contributed from the outmost atoms of the ribbon upper or lower edge is verified

according to the LDOS. However, under a small off-plane field the shuttle-shape bands are easily separated into two degenerated near-flat bands contributed from the edge atoms of the top or bottom sublayer. The edge band variation with external field for this category is completely different from that of (2,4)PNR belonging to previously reported zPNR category. This is because a (1,3)PNR has four zigzag atomic configurations on the upper and lower edges and the degenerate bands are from the outermost atoms in the same sublayer or different upper-lower edge. This allows the two DOFs to be distinguished and regulated by applying electric field along different directions. Further, based on this issue we propose a (1,3)PNR homogenous junction attached by electric gates. Interestingly, the transport property of the junction with field manipulation well reflects the characteristics of the two DOFs for (1,3)PNR category. In addition, the defect effect from the vacancies in edge and bulk on the transport property is also discussed. These results may provide a further understanding on PNRs and initiate new developments in PNR-based electronics.

ACKNOWLEDGMENTS

[1] K. S. Novoselov, A. K. Geim, S. V. Morozov, D. Jiang, Y. Zhang, S. V. Dubonos, I. V. Grigorieva, and A. A. Firsov, Science **306**, 666 (2004).

[2] K. F. Mak, C. Lee, J. Hone, J. Shan, and T. F. Heinz, Phys. Rev. Lett. **105**, 136805 (2010).

[3] P. San-Jose, E. Prada, E. McCann, and H. Schomerus, Phys. Rev. Lett. **102**, 247204 (2009).

[4] X. Xu, W. Yao, D. Xiao, and T. F. Heinz, Nat. Phys. **10**, 343 (2014).

[5] S. Soleimanikahnoj and I. Knezevic, Phys. Rev. Appl. **8**, 064021 (2017).

[6] Y. Ren, P. Liu, B. Zhou, X. Zhou, and G. Zhou, Phys. Rev. Appl. **12**, 064025 (2019).

[7] L. Li, Y. Yu, G. J. Ye, Q. Ge, X. Ou, H. Wu, D. Feng, X. H. Chen, and Y. Zhang, Nat. Nanotechnol. **9**, 372 (2014).

[8] X. Ling, H. Wang, S. Huang, F. Xia, and M. S. Dresselhaus, Proc. Natl. Acad. Sci. USA **112**, 4523 (2015).

[9] C. Q. Han, M. Y. Yao, X. X. Bai, L. Miao, F. Zhu, D. D. Guan, S. Wang, C. L. Gao, C. Liu, D. Qian, Y. Liu, and J.-f. Jia, Phys. Rev. B **90**, 085101 (2014).

[10] A. Carvalho, A. S. Rodin, and A. H. Castro Neto, Europhys. Lett. **108**, 47005 (2014).

[11] Likai Li, J. Kim, C. Jin, G. Ye, D. Y. Qiu, Felipe H. da Jornada, Z. Shi, L. Chen, Z. Zhang, F. Yang, K. Watanabe, T. Taniguchi, W. Ren, S. G. Louie, and X. Chen, Y. Zhang, and F. Wang, Nat. Nanotechnol. **12**, 21 (2017).

[12] S. P. Koenig, R. A. Doganov, H. Schmidt, A. H. Castro Neto, and B. Özyilmaz, Appl. Phys. Lett. **104**, 103106 (2014).

[13] Michele Buscema, D. J. Groenendijk, S. I. Blanter, G. A. Steele, Herre S. J. van der Zant, and A. Castellanos-Gomez, Nano Lett. **14**, 3347 (2014).

[14] F. Xia, H. Wang, and Y. Jia, Nat. Commun. **5**, 4458 (2014).

[15] S. J. R. Tan, I. Abdelwahab, L. Chu, Sock M. Poh, Y. Liu, J. Lu, W. Chen, and K. P. Loh, Adv. Mater. **30**, 1704619 (2018).

[16] H. Liu, A. T. Neal, Z. Zhu, Z. Luo, X. Xu, D. Tománek, and P. D. Ye, ACS Nano **8**, 4033 (2014).

[17] P. Li and I. Appelbaum, Phys. Rev. B **90**, 115439 (2014).

[18] X. Zhou, W.-K. Lou, D. Zhang, F. Cheng, G. Zhou, and K. Chang, Phys. Rev. B **95**, 045408 (2017).

[19] X. Y. Zhou, R. Zhang, J. P. Sun, Y. L. Zou, D. Zhang, W. K. Lou, F. Cheng, G. H. Zhou, F. Zhai, and K. Chang, Sci. Rep. **5**, 12295 (2015).

[20] P. Liu, X. Zhu, X. Zhou, G. Zhou, and K. Chang, Sci. China-Phys. Mech. Astron. **64**, 217811 (2021).

[21] P. M. Das, G. Danda, A. Cupo, W. M. Parkin, L. Liang, N. Kharche, X. Ling, S. Huang, M. S. Dresselhaus, V. Meunier, and M. Drndic, ACS Nano **10**, 5687 (2016).

[22] M. C. Watts, L. Picco, F. S. Russell-Pavier, P. L. Cullen1, thomas S. Miller, S. P. Bartuś, O. D. Payton, N. T. Skipper, V. Tileli, and C. A. Howard, Nature (London) **568**, 216 (2019).

[23] V. Tran and L. Yang, Phys. Rev. B **89**, 245407 (2014).

[24] M. Ezawa, New J. Phys. **16**, 115004 (2014).

[25] R. Zhang, X. Y. Zhou, D. Zhang, W. K. Lou, F. Zhai, and K. Chang, 2D Mater. **2**, 045012 (2015).

[26] A. Maity, A. Singh, P. Sen, A. Kibey, A. Kshirsagar, and D. G. Kanhere, Phys. Rev. B **94**, 075422 (2016).

[27] M. M. Grujić, M. Ezawa, Milan Ž. Tadić, and F. M. Peeters, Phys. Rev. B **93**, 245413 (2016)

[28] B. Zhou, B. Zhou, X. Zhou, and G. Zhou, J. Phys. D: Appl. Phys. **50**, 045106 (2017).

[29] K. Nakada, M. Fujita, G. Dresselhaus, and M. S. Dresselhaus, Phys. Rev. B **54**, 17954 (1996).

[30] M. V. Bollinger, J. V. Lauritsen, K. W. Jacobsen, J. K. Nørskov, S. Helveg, and F. Besenbacher, Phys. Rev. Lett. **87**, 196803 (2001).

[31] D. J. P. de Sousa, L. V. de Castro, D. R. da Costa, and J. M. Pereira, J. Phys. Rev. B **94**, 235415 (2016).

[32] SK F. Islam, P. Dutta, A. M. Jayannavar, and A. Saha, Phys. Rev. B **97**, 235424 (2018).

[33] Y. Ren, F. Cheng, Z. H. Zhang, and G. Zhou, Sci. Rep. **8**, 2932 (2018).

[34] E. Taghizadeh Sisakht, F. Fazileh, M. H. Zare, M. Zarenia, and F. M. Peeters, Phys. Rev. B **94**, 085417 (2016).

[35] A. Ramasubramaniam and A. R. Muniz, Phys. Rev. B **90**, 085424 (2014).

[36] Y. Liu, F. Xu, Z. Zhang, E. S. Penev, and B. I. Yakobson, Nano Lett. **14**, 6782 (2014).

[37] Y. Lee, S. Lee, J.-Y. Yoon, J. Cheon, H. Y. Jeong, and K. Kim, Nano Lett. **20**, 559 (2020).

[38] L. Liang, J. Wang, W. Lin, B. G. Sumpter, V. Meunier, and M. Pan, Nano Lett. **14**, 6400 (2014).

[39] B. Kiraly, N. Hauptmann, A. N. Rudenko, M. I. Katsnelson, and A. A. Khajetoorians, Nano Lett. **17**, 3607 (2017).

[40] L. L. Li and F. M. Peeters, Phys. Rev. B **97**, 075414 (2018).

[41] C. W. Groth, M. Wimmer, A. R. Akhmerov, and X. Waintal, New J. Phys. **16**, 063065 (2014).

[42] Y. Jiang and L. Hu, Phys. Rev. B **75**, 195343 (2007).

[43] M. Zwierzycki, P. A. Khomyakov, A. A. Starikov, K. Xia, M. Talanana, P. X. Xu, V. M. Karpan, I. Marushchenko, I. Turek, G. E. W. Bauer, G. Brocks, and P. J. Kelly, Phys. Stat. Sol. B **245**, 623 (2008).

[44] T. P. Santos, Leandro R. F. Lima, C. H. Lewenkopf, J. Comput. Phys. **394**, 440 (2019).

[45] A. N. Rudenko and M. I. Katsnelson, Phys. Rev. B **89**, 201408(R) (2014).

[46] S. Smidstrup, T. Markussen, P. Vancraeyveld, J. Wellendorff, J. Schneider, T. Gunst, B. Verstichel, D. Stradi, P. A. Khomyakov, and U. G. Vej-Hansen, J. Phys.: Condens. Matter **32**, 015901 (2020).

[47] S. Datta, *Electronic Transport in Mesoscopic Systems* (Cambridge University Press, Cambridge, 1995).

[48] H. Guo, N. Lu, J. Dai, X. Wu, and X. C. Zeng, J. Phys. Chem. C **118**, 14051 (2014).

[49] D. Zhang, W. Lou, M. Miao, S.-c. Zhang, and K. Chang, Phys. Rev. Lett. **111**, 156402 (2013).

[50] Z. Li, H. Qian, J. Wu, B. L. Gu, and W. Duan, Phys. Rev. Lett. **100**, 206802 (2008).

[51] J. Kang, F. Wu, and J. Li, Appl. Phys. Lett. **100**, 233122 (2012).

[52] B. Hähnlein, B. Hündel, J. Pezoldt, H. Töpfer, R. Granzner, and F. Schwierz, Appl. Phys. Lett. **101**, 093504 (2012).

[53] F. Molitor, J. Guttinger, C. Stampfer, D. Graf, T. Ihn, and K. Ensslin, Phys. Rev. B **76**, 245426 (2007).

[54] V. Tayari, N. Hemsworth, O. Cyr-Choinière, W. Dickerson, G. Gervais, and T. Szkopek, Phys. Rev. Applied **5**, 064004 (2016).

[55] J. S. Kim, P. J. Jeon, J. Lee, K. Choi, H. S. Lee, Y. Cho, Y. T. Lee, D. K. Hwang, and S. Im, Nano Lett. **15**, 5778 (2015).